Multiple-Well, Multiple-Path Unimolecular Reaction Systems. II. 2-Methylhexyl Free Radicals

JOHN R. BARKER[1] AND NICOLAS F. ORTIZ[2]

[1]*Department of Atmospheric, Oceanic, and Space Sciences, Department of Chemistry, University of Michigan, Ann Arbor,* MI 48109-2143

[2]*Department of Chemical Engineering, University of Michigan, Ann Arbor,* MI 48109

Received 5 July 2000; accepted 16 October 2000

ABSTRACT: Vibrationally excited 2-methylhexyl radicals formed by shock wave activation or by chemical activation can isomerize by multiple pathways to form any of six stable isomers, can fragment by multiple C—H and C—C bond fission pathways, and can be collisionally stabilized. Master equation simulations of chemical activation and of shock wave activation are used to explore the generic behavior of this complicated coupled system. Selecting the argon pressure in chemical activation systems that produce the 2-methyl-1-hexyl radical isomer (**1**) can control the yield of specific isomers. Shock heating of **1** also shows a highly regular sequence of isomer formation. This regular behavior is because the first isomerization steps are faster than subsequent steps. Other radical isomers, such as 2-methyl-3-hexyl (**3**), do not show such regular behavior, because the first isomerization step is slower than subsequent steps. Incubation and unimolecular rate-constant fall-off are observed in the shock wave simulations. The unimolecular rate-constant fall-off for the coupled system produces low-pressure limiting rate constants proportional to $[M]^n$, where n can be greater than unity. The fact that n can be greater than unity is a natural feature of multichannel coupled unimolecular reaction systems, but detection of the effect in experiments may be very demanding. Int J Chem Kinet 33: 246–261, 2001

INTRODUCTION

Unimolecular reaction systems with multiple isomers that are connected by multiple isomerization pathways and that may react by multiple fragmentation pathways are common in pyrolysis and combustion chemistry. Alkyl radicals (R•) that contain at least two carbon atoms isomerize by means of the free radical center's abstracting a hydrogen atom from a site further along the carbon chain: an intramolecular metathesis reaction. They fragment by C—C and C—H bond fission to produce R• + olefin or H + olefin products, respectively. Alkoxy (RO•) radicals and peroxy (RO_2•) radicals, which are important in atmospheric and combustion oxidation systems, undergo analogous reactions.

The isomerization and fragmentation reactions of alkyl radicals are of great importance because the activation barriers are low and hence the reactions are rapid under conditions that are readily achieved in common chemical systems, such as combustion and atmospheric photooxidation. Furthermore, the rates of isomerization and fragmentation are competitive, leading to complicated mixtures of products. Modeling these systems can become extremely complicated be-

Correspondence to: J. R. Barker (jrbarker@unmich.edu)

cause the reactions have energy-dependent rate coefficients and collisional activation and deactivation must be taken into account. In the preceding article (Article I) [1], a computer code, MultiWell [2], is described that was specifically designed for master equation simulations of systems like these.

In the following sections, the 2-methylhexyl (2MH) radical system is described, followed by a description of technical aspects of the master equation simulations. The results of two types of simulations are then summarized: chemical activation excitation, such as might occur in a photochemical system, and shock-induced reaction, such as would occur in shock tube experiments and in other extreme environments. Results and conclusions are summarized in the final section.

THE 2-METHYLHEXYL RADICAL SYSTEM

Recently, Viskolzc et al. [3] reported *ab initio* calculations of structures and energies of the isomers and isomerization transition states for the 2MH free radical system, a prototype for alkyl radicals. In the absence of isotopic substitution, this system consists of six stable chemical isomers that can isomerize via 3-, 4-, 5-, 6-, or 7-membered ring transition states for a total of 15 reversible isomerization reactions. Viskolcz et al. did not consider the fragmentation reactions, which are at slightly higher energies, but Yamauchi et al. [4] investigated such reactions for a series of alkyl radicals both experimentally and theoretically and gave recommendations for high-pressure-limit Arrhenius parameters. In the 2MH system, each isomer can fragment via at least two pathways to produce 14 distinct sets of products (the distinction between *cis* and *trans* olefins is neglected throughout this article). All of the isomers (6), all of the isomerization pathways (30), and all of the fragmentation pathways (19) were used simultaneously in the master equation calculations described here.

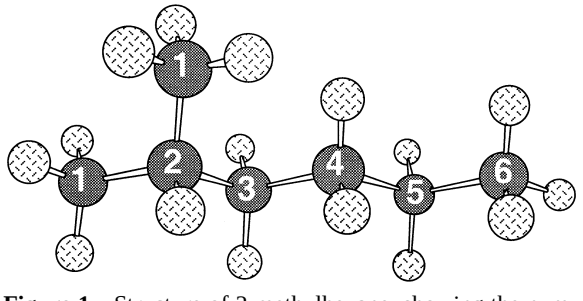

Figure 1 Structure of 2-methylhexane, showing the numbering scheme for free-radical sites.

Table I Properties of 2-Methylhexyl Radical Isomers [3]

Isomer	ΔH_f°(0 K) kcal mole^{-1}	$\mathbf{I}_A$ amu Å^2	σ_{ext}	g_e	m
1	3.53	521.	1	2	2
2	0.00	528.	1	2	1
3	1.29	537.	1	2	2
4	1.11	528.	1	2	2
5	1.12	530.	1	2	2
6	3.00	516.	1	2	1

See Eq. (1) and text for definitions.

Relatively little experimental work has been done on the isomerization and fragmentation of alkyl radicals (see Viskolzc et al. [3] for references). Experiments have been reported on the 2MH system involving the reactions of chemically activated 2-methyl-3-hexyl radicals in a collisional bath of H_2 [5], as discussed in a later section.

Isomers

For convenience, the isomers in the 2MH system are labeled according to the carbon atom where the free radical site resides. For example, **1** is the 2-methyl-1-hexyl radical with the free radical site on carbon #1. The numbering system is shown in Figure 1, where radicals are produced by removing a hydrogen atom from any one of the six chemically distinguishable carbon atoms. In Table I are listed values of the enthalpy of formation relative to the most stable isomer (ΔH_f°(0 K)), moment of inertia for the two-dimensional external rotor (I_A), the external rotational symmetry number (σ_{ext}), the electronic degeneracy (g_e), and the number of optical isomers (m) for each geometrical isomer. All of these quantities are derived from the *ab initio* calculations of Viskolcz et al. [3]. Because of internal rotation, each isomer has many possible conformations, each with its own moment of inertia I_A. For present purposes, this variation was neglected, and for each structural isomer all conformations of all optical isomers were assumed to have the same moment of inertia.

Vibrational frequencies for each vibrational structure were calculated by Viskolcz et al. [3] and were communicated by G. Lendvay [6]. The vibrational frequencies were scaled by the usual factor [7] of 0.8929 before being used in calculating sums and densities of vibrational states. Sample calculations of specific unimolecular rate constants ($k(E)$'s) showed that rate constants calculated with, and without, the scaling fac-

tor were practically identical. Although many of the low-frequency vibrations can be identified with torsions and hindered free rotors, we used strictly vibrational models in the present work. The replacement of some low-frequency vibrations by torsions can affect the numerical results but will not affect any of the qualitative conclusions, which are the focus of this work.

Reactions and Transition States

The reactions in the 2MH system are summarized in Figure 2, where the lines indicate isomerization and fragmentation pathways. Viskolcz et al. [3] reported activation barriers and structures for all of the isomerization pathways (see Table II), and Lendvay communicated the vibrational frequencies calculated in that work [6]. The properties of the isomerization transition states are summarized in Table II, where the ‡ superscript denotes the transition state. Note that the isomers have slightly different energies (ΔH_f°(0 K) and the pathways have significantly different energy barriers to reaction, as shown in Figure 3 for **1.** All of the isomerization reactions have significant energy barriers, and thus fixed (tight) transition states are appropriate [8–11].

All of the master equation calculations described below were carried out using standard features of MultiWell (Article I). The specific rate constants were calculated according to RRKM theory for the 30 energy-dependent unimolecular isomerization reactions. Once again, the vibrational frequencies were scaled by the factor [7] of 0.8929. According to RRKM theory, the specific rate constant is given by [8–11]

$$k(E) = \left[\frac{m^\ddagger}{m}\frac{\sigma_{\text{ext}}}{\sigma_{\text{ext}}^\ddagger}\right]\frac{g_e^\ddagger}{g_e}\frac{1}{h}\frac{G^\ddagger(E-E_0)}{\rho(E)} \qquad (1)$$

where $m^\ddagger$ and m are the numbers of optical isomers [10]; $\sigma_{\text{ext}}{}^\ddagger$ and σ_{ext} are the external rotation symmetry numbers; $g_e{}^\ddagger$ and g_e are the electronic state degeneracies of the transition state and reactant, respectively; h is Planck's constant; $G^\ddagger(E - E_0)$ is the sum of states of the transition state; E_0 is the reaction threshold energy; and $\rho(E)$ is the density of states of the reactant molecule. The internal energy E is measured relative to the zero-point energy of the reactant molecule, and the reaction threshold energy (critical energy) is the difference between the zero-point energies of reactant and transition state.

Fragmentation of alkyl radicals can take place via C—H and C—C bond fission to produce the products summarized in Table III. A recent paper by Yamauchi

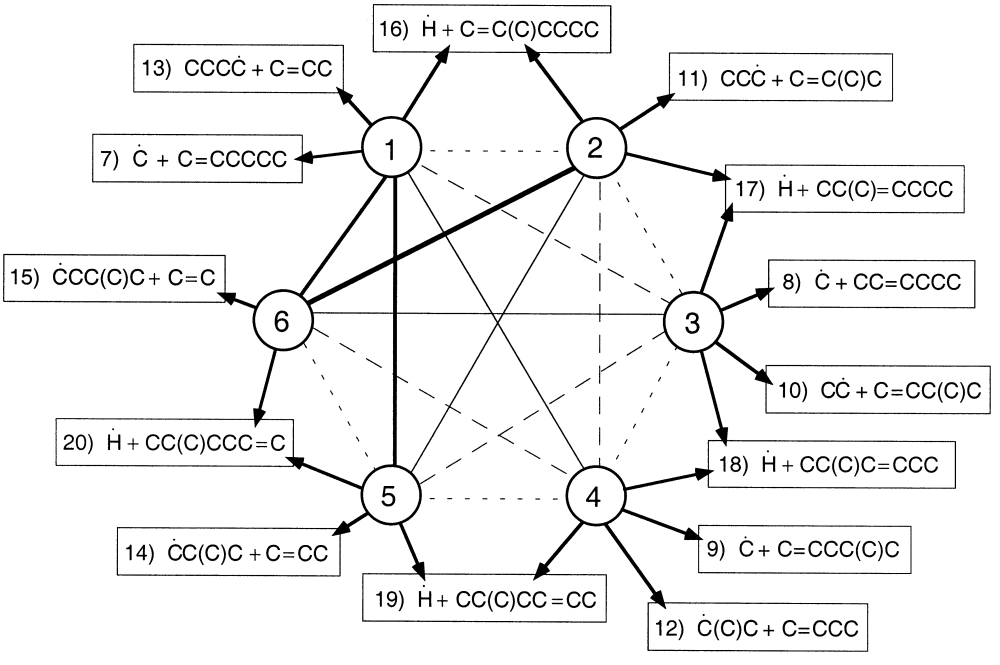

Figure 2 Schematic reaction mechanism for 2-methylhexyl radical isomerization and fragmentation. Reversible isomerization reactions are shown by solid and dashed lines connecting the circles that represent each of the six isomers. Thick solid lines: 6-membered-ring cyclic transition states; thin solid lines: 5- and 7-membered rings; long dashes: 4-membered rings; short dashes: 3-membered rings. Fragmentation products (in boxes) are numbered according to Table III.

Table II Isomerization Reactions[a]

From	To	Transition State	$I_A^{\ddagger}$ amu Å^2	$\sigma_{ext}^{\ddagger}$	$g_e^{\ddagger}$	$m^{\ddagger}$	E_0[b] kcal mole^{-1}	A_∞[b,c] s^{-1}	A_∞[c,d] s^{-1}	E_∞[d] kcal mole^{-1}
1	**2**	2MH-1-02	524.	1	2	2	36.46	9.6 (12)	9.1 (12)	36.8
1	**3**	2MH-1-03	523.	1	2	4	38.12	7.9 (12)	1.4 (13)	38.3
1	**4**	2MH-1-04	429.	1	2	4	20.59	9.8 (11)	1.8 (12)	20.5
1	**5**	2MH-1-05	388.	1	2	4	13.43	3.0 (11)	7.2 (11)	13.2
1	**6**	2MH-1-06	339.	1	2	2	15.14	1.4 (11)	1.4 (11)	14.7
3	**2**	2MH-3-02	529.	1	2	2	38.56	7.6 (12)	4.9 (12)	39.0
4	**2**	2MH-4-02	433.	1	2	2	37.37	1.0 (12)	2.0 (12)	37.6
4	**3**	2MH-4-03	530.	1	2	4	38.32	1.6 (12)	6.0 (12)	38.6
5	**2**	2MH-5-02	248.	1	2	2	19.53	5.2 (11)	7.5 (11)	19.8
5	**3**	2MH-5-03	427.	1	2	4	39.02	2.2 (12)	8.8 (12)	39.2
5	**4**	2MH-5-04	526.	1	2	4	38.38	4.1 (12)	1.6 (13)	38.7
6	**2**	2MH-6-02	300.	1	2	1	12.11	3.8 (11)	3.2 (11)	12.0
6	**3**	2MH-6-03	359.	1	2	2	21.51	7.4 (11)	1.4 (12)	21.4
6	**4**	2MH-6-04	462.	1	2	2	38.17	5.4 (12)	9.9 (12)	38.3
6	**5**	2MH-6-05	519.	1	2	2	38.59	6.2 (12)	1.2 (13)	38.9

[a] See Eq. (1) and text for definitions.
[b] Viskolcz et al. [3].
[c] Notation: 9.55 (12) = 9.55×10^{12}.
[d] This work (evaluated at 300 K).

et al. reports experiments and *ab initio* calculations on alkyl radical decomposition and fragmentation reactions [4]. Their results are in generally good agreement with other experimental work and with estimation methods like those described by Benson [12]. High-pressure-limit rate constants for the decomposition reactions tabulated in Table I of the paper by Yamauchi et al. were used to estimate the parameters presented in Table IV, where A_∞ is the high-pressure-limit A-factor and E_0 is the estimated critical energy for each of the 19 fragmentation reactions. Note that the number of optical isomers ($m^{\ddagger}$) of each transition state is the same as that for the reactant. All of the fragmentation reactions were included in the calculations.

The specific rate constants for all of the fragmentation reactions were calculated using the results from Yamauchi et al. [4], as given in Table IV. Because vibrational frequencies were not reported by Yamau-

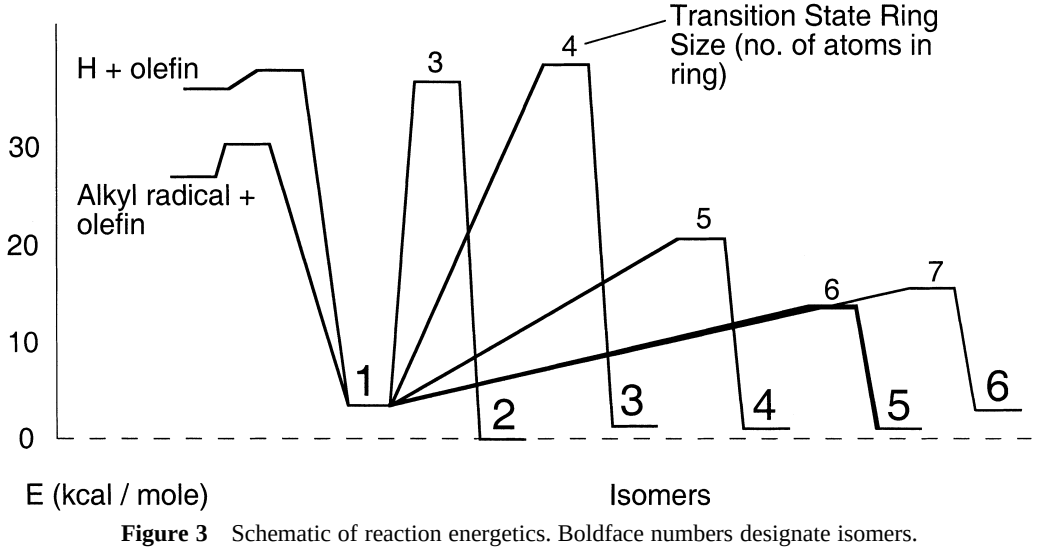

Figure 3 Schematic of reaction energetics. Boldface numbers designate isomers.

Table III Fragmentation Product Sets [3]

Number	Product Set[a]
7	$\dot{C}$ + C = CCCCC
8	$\dot{C}$ + CC = CCCC
9	$\dot{C}$ + C = CCC(C)C
10	C$\dot{C}$ + C = CC(C)C
11	C$\dot{C}$C + C = C(C)C
12	$\dot{C}$(C)C + C = CCC
13	C$\dot{C}$CC + C = CC
14	$\dot{C}$C(C)C + C = CC
15	$\dot{C}$CC(C) + C = C
16	$\dot{H}$ + C = C(C)CCCC
17	$\dot{H}$ + CC(C) = CCCC
18	$\dot{H}$ + CC(C)C = CCC
19	$\dot{H}$ + CC(C)CC = CC
20	$\dot{H}$ + CC(C)CCC = C

[a] Notation: i-propyl radical: $\dot{C}$(C)C; 2-methyl-1-hexene: C = C(C)CCCC.

chi et al., it was convenient to estimate the specific rate constants by using the inverse Laplace transform expression described by Forst, in which strict Arrhenius behavior is assumed for the high-pressure-limit rate constant [9,13]:

$$k(E) = \left[\frac{m^{\ddagger}}{m}\frac{\sigma_{\text{ext}}}{\sigma_{\text{ext}}^{\ddagger}}\right]A_{\infty}\frac{\rho(E-E_{\infty})}{\rho(E)} \qquad (2)$$

where A_∞ and E_∞ are the Arrhenius A-factor (preexponential factor) and activation energy, respectively, for the high-pressure-limit thermal rate constant. This is a convenient and reasonably accurate approximation that is suitable for use when a detailed vibrational assignment of the transition state is not available. In order to improve accuracy just above the reaction threshold, the high-pressure-limit activation energy (E_∞) was replaced in Eq. (2) by the reaction critical energy (E_0). This replacement is expected to improve the accuracy of thermal rate constants in the fall-off, but the high-pressure-limit activation energy will be affected slightly.

Whether $k(E)$ is evaluated according to Eq. (1) or according to Eq. (2), the unimolecular rate constant at the high pressure limit $k_\infty(T_{\text{trans}})$ can be expressed in terms of $\rho(E)$ and $k(E)$:

$$k_{\infty}(T_{\text{trans}}) = \frac{1}{Q(T_{\text{trans}})}\int_{E_0}^{\infty}k(E)\rho(E)\exp(-E/k_{\text{B}}T_{\text{trans}})dE \qquad (3)$$

where $Q(T_{\text{trans}})$ is the partition function of the reactant

Table IV Fragmentation Reactions [4]

From	To	Transition State	$m^{\ddagger}$	E_0 kcal mole^{-1}	A_∞[a,b] s^{-1}
1	**7**	2MH-1-07	2	30.0	1.0 (13)
1	**13**	2MH-1-13	2	30.0	1.0 (13)
1	**16**	2MH-1-16	2	37.5	7.0 (13)
2	**11**	2MH-2-11	1	30.0	1.0 (13)
2	**16**	2MH-2-16	1	37.5	7.0 (13)
2	**17**	2MH-2-17	1	37.5	2.1 (14)
3	**8**	2MH-3-08	2	30.0	1.0 (13)
3	**10**	2MH-3-10	2	30.0	1.0 (13)
3	**17**	2MH-3-17	2	37.5	7.0 (13)
3	**18**	2MH-3-18	2	37.5	1.4 (14)
4	**9**	2MH-4-09	2	30.0	1.0 (13)
4	**12**	2MH-4-12	2	30.0	1.0 (13)
4	**18**	2MH-4-18	2	37.5	1.4 (14)
4	**19**	2MH-4-19	2	37.5	1.4 (14)
5	**14**	2MH-5-14	2	30.0	1.0 (13)
5	**19**	2MH-5-19	2	37.5	2.1 (14)
5	**20**	2MH-5-20	2	37.5	1.4 (14)
6	**15**	2MH-6-15	1	30.0	1.0 (13)
6	**20**	2MH-6-20	1	37.5	1.4 (14)

[a] Notation: 1.0 (13) = 1.0×10^{13}.

[b] Note that $E_\infty = E_0$ (according to the present version of the inverse Laplace transform expression for $k(E)$).

internal degrees of freedom (the degrees of freedom used to calculate $\rho(E)$ and $k(E)$) at translational temperature T_{trans}:

$$Q(T_{trans}) = \int_0^\infty \rho(E)\exp(-E/k_B T_{trans})dE \qquad (4)$$

In MultiWell, the integrals in Eqs. (4) and (5) are carried out numerically and the activation energy is obtained by calculating $k_\infty(T_{trans})$ at two closely spaced temperatures:

$$E_\infty = -R\frac{\ln[k_\infty(T_2)/k_\infty(T_1)]}{[T_2^{-1} - T_1^{-1}]} \qquad (5)$$

From the E_∞ and the k_∞ at one temperature, the A-factor (A_∞) can be calculated. Values for E_∞ and A_∞ calculated in this way at $T_{trans} = 300$ K are reported for each reaction in Tables II and IV. The results obtained in this way for reactions where $k(E)$ was calculated via Eq. (2) agree within 0.1% with the original input data (A_∞ and E_0), which should be recovered by this numerical procedure. This level of agreement is quite satisfactory, confirming the accuracy of the numerical techniques.

As shown in Table II, the values of A_∞ obtained in the present work differ from those reported by Viskolcz et al., which were not described in detail but were apparently obtained using statistical mechanics formulas [3]. In most cases, the ratios of the present results to those reported by Viskolcz are approximately, but not exactly, integers. The specific reasons for the differences are not known, but there are several possible contributions. First, the $k(E)$ values were calculated in the present work from exact counts of states (10 cm^{-1} grain size) and numerical integration of Eqs. (3) and (4), instead of from the statistical mechanics formulas used by Viskolcz et al. Numerical tests using $k(E)$ from Eq. (2) showed that the numerical methods are accurate to within a small fraction of 1%. Thus, the numerical techniques do not introduce significant errors. Second, the statistical factors (see Eqs. (1) and (2)) that were used in the present work included optical isomers. Viskolcz et al. do not mention whether they considered the optical isomers. If they did not, then this omission can explain most, but not all, of the near-integer ratios. In those few remaining cases, we have no explanation for the discrepancies.

Collisional Energy Transfer

All of the simulations were carried out by assuming that the 2MH radicals are diluted in an infinite excess of argon. The collision frequency was calculated assuming a Lennard-Jones interaction potential [14]. The Lennard-Jones parameters for the free radicals were assumed to be identical to those for 2-methylhexane, which were estimated [15] from the critical properties. The critical properties for 2-methylhexane were estimated using the formulas [15] of Miller (for T_C), Lydersen (for P_C), and Vetere (for V_C). The resulting values for the estimated critical properties and Lennard-Jones parameters are listed in Table V.

Table V Parameters for 2-Methylhexane and Argon

Parameter	Value
2-Methylhexane (see text for details)	
T_C	538.22 K
P_C	27.41 atm
V_C	422.83 cm^3 $mole^{-1}$
Z_C	0.262
σ	7.61 Å
ε/k_B	284.6 K
Argon	
σ	3.655 Å
ε/k_B	178.9 K

Energy transfer data are not available for the 2MH system. As discussed elsewhere [16], energy transfer data for large molecules are scanty and of uneven quality. When faced with the necessity of estimating energy transfer parameters that have never been measured, a reasonable approach is to adopt the parameters corresponding to an analogous compound, when possible. Almost all systems that have been studied by physical ("direct") techniques consist of substituted aromatics, and it has been found that internal rotation significantly affects energy transfer parameters [17–19]. 2MH radicals contain low-frequency (torsional) vibrations, and thus we selected toluene as an analogue. Toluene contains an internal rotor, and its energy transfer properties have been measured by the two most accurate experimental techniques currently available.

The toluene energy transfer properties measured by the infrared fluorescence (IRF) technique [17,18] were fitted using the exponential and biexponential models for collisional energy transfer. Those measured by the kinetically controlled selective ionization (KCSI) method [20] are based on a generalized version of the exponential model, described by the following expression for the collision step-size distribution for deactivation steps [21]:

$$f_d(E, E') = \exp\left\{-\left|\frac{E'-E}{\alpha(E')}\right|^\gamma\right\}, \quad \text{for } E' > E \qquad (6)$$

Table VI Energy Transfer Parameters (see text for details)

Experimental Method	γ	$\alpha(E)$, cm^{-1}	Reference
IRF	1.0	$36 + 0.009 \times E$	18
KCSI	0.7	$43.5 + 0.0042 \times E$	20

where $\alpha(E)$ is a linear function of vibrational energy and γ is a parameter that ranges from ~0.5 to ~1.5. The corresponding expression for activation collisions is obtained from detailed balance according to Eq. (4). When the parameter γ is less than unity, the wings of the step-size distribution have enhanced relative probabilities that qualitatively resemble the biexponential distribution. When $\gamma = 1$, Eq. (18) gives the exponential model. For more details, see Article I and [16]. In order to determine how the choice of energy transfer model can affect master equation simulations, we carried out calculations using a simple exponential model with parameters derived from IRF data and using the generalized exponential model with parameters derived from KCSI experiments (Table VI). Note that the KCSI technique is currently thought to be more accurate than other methods [16].

NUMERICAL SOLUTION OF THE MASTER EQUATION

The master equation for multiple-well, multiple-channel reaction systems is highly complicated, especially when collisional energy transfer is included. One of the purposes of the present work is to demonstrate the capabilities of MultiWell [1], a new computer program that was designed to handle such problems without the need for recompiling or restructuring the code. This code is publicly available from the author or by downloading from a website [2]. In brief, MultiWell is a significant extension of codes previously developed in our laboratory [22–26]. It is based on an exact stochastic algorithm, which Gillespie showed to be mathematically equivalent to the set of integro-differential equations that comprise the master equation [27–29]. Article I [1] should be consulted for a complete description of the numerical details and of the strengths and weakness of the method.

RESULTS

Chemical Activation

In chemical activation, an exothermic chemical reaction generates excited species by the following [5,30,31]. In the 2MH system, two types of chemical activation processes are possible:

$$\mathrm{H\bullet} + \text{Olefin} \rightarrow \mathrm{R\bullet^*} \qquad E_0 \approx 37 \text{ kcal mole}^{-1} \quad (7)$$

$$\mathrm{R'\bullet} + \text{Olefin} \rightarrow \mathrm{R\bullet^*} \qquad E_0 \approx 30 \text{ kcal mole}^{-1} \quad (8)$$

where the asterisk denotes vibrational excitation; the approximate threshold energies (E_0) for the reverse reactions [4] are shown. The nascent energy distribution [8–10] of excited radicals, which is relatively narrow, can be calculated using $k_i(E)$ for the reverse reaction (i designates the reaction channel):

$$y_0^{(ca,i)}(E)dE = \frac{k_i(E)\rho(E)\exp(-E/k_B T_{vib})\,dE}{\int_{E_0}^{\infty} k_i(E')\rho(E')\exp(-E/k_B T_{vib})\,dE'} \quad (9)$$

where $\rho(E)$ is the density of states, E_0 is the threshold energy, $k_i(E)$ is the specific rate constant for ith decomposition reaction, and k_B is the Boltzmann constant.

Convergence Tests. As described in Article I, several parameters are needed for the numerical solution of the master equation. For example, the vibrational energies spanned in the simulations should not exceed the maximum energy (E_{max}) specified for the numerical solution using MultiWell [2]. MultiWell is based on a "hybrid" formulation of the numerical master equation. According to this approach, the low energy range is treated effectively with an energy-grained master equation and the high energy range is treated with a continuum master equation, as described in Article I. The energy separating the two energy ranges must lie above the sparse states regime. Most important, the energy grain size (ΔE_{grain}) for the low energy range must be small enough so that the sparse states regime is accurately represented. Here, the "sparse states regime" refers to the widely separated states near the bottom of a potential well as well as to the widely separated states of the transition state at energies just above a reaction threshold energy. In the sparse states regime at low energies within a well, collisional energy transfer is slow because the states are widely separated, necessitating large energy transfer steps. Furthermore, the unimolecular rate constant varies dramatically in the sparse states regime just above a reaction threshold.

In the limit of very small ΔE_{grain} and very high E_{max}, numerical accuracy is maximized, as are the demands on computer time and storage. By carrying out tests, it is possible to determine simulation parameters that do not compromise accuracy and yet are not so de-

manding on computer time. In all of the calculations reported here, $E_{max} = 85{,}000\ cm^{-1}$. Preliminary results showed that only a vanishingly small population occurred at energies higher than 50,000 cm^{-1}, and increasing E_{max} from 85,000 cm^{-1} to 100,000 cm^{-1} had no effect on the results. Similarly, tests showed that a dividing line between the high and low energy regimes set at $\sim$2500 cm^{-1}, where the state densities are almost continuous (i.e., the vibrational quasicontinuum), gave results indistinguishable from a dividing line set at 3000 cm^{-1}.

The variation of test results for ΔE_{grain} are shown in Figure 4 for chemical activation (via the reaction H + 2-methyl-hexene-1) at 300 K and a number density of 1.5×10^{12} cm^{-3} of argon collider. The duration of the simulated experiments was 0.001 s, corresponding to 966 collisions, which was more than enough for collisional stabilization of those isomers that did not decompose. In these tests, the dividing line between the low and high energy regimes was given by $249 \times \Delta E_{grain}$. The "relative yield" in Figure 4 is the yield of a particular species or product set relative to the yield when $\Delta E_{grain} = 5\ cm^{-1}$. For the 2MH system, the relative yields have converged to the limit (within the statistical uncertainties) for $\Delta E_{grain} \leq 50\ cm^{-1}$. In all subsequent simulations, we have used $\Delta E_{grain} = 10\ cm^{-1}$.

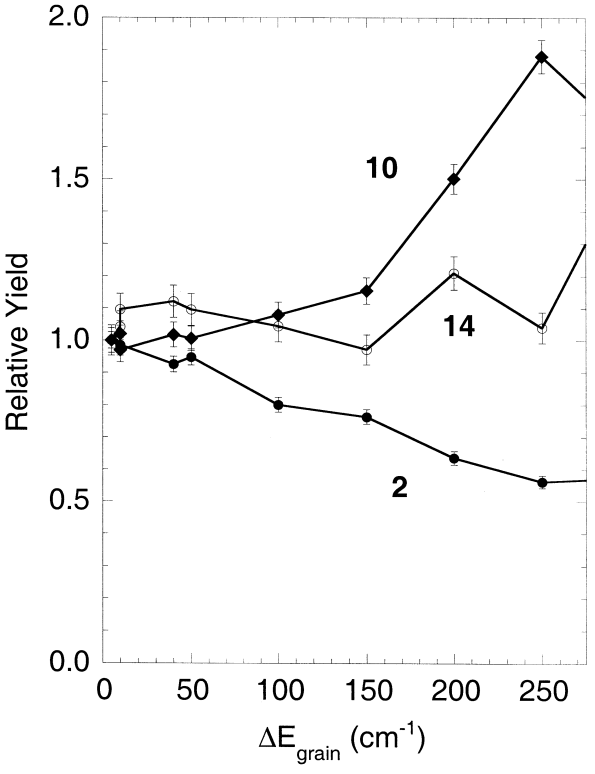

Figure 4 Convergence tests for energy grain size. Boldface numbers designate isomers and reaction product sets.

Chemical Activation Simulations. Figure 2 shows the many chemical activation pathways available for study in this system. In many cases, a single set of reactants can lead to two of the 2MH radical isomers because of addition to either end of a double bond. For example,

$$H + \text{2-methyl-1-hexene} \rightarrow \mathbf{1} \qquad (10a)$$

$$\rightarrow \mathbf{2} \qquad (10b)$$

Formation of the tertiary radical (**2**) is strongly favored (Markownikoff addition) over the primary radical (anti-Markownikoff addition) due to a difference in activation energy [30,12]. Similar behavior is expected for Reactions (7) and (8). Both **1** and **2** can isomerize readily via both 5- and 6-membered-ring cyclic transition states, which have low energy barriers. The same is true of **5** and **6,** in contrast with **3** and **4,** which have only a single 5-membered-ring transition state reaction path available to each of them.

To explore the behavior of radicals with one rapid isomerization pathway and those with more than one, we carried out simulations of several chemical activation systems. These included examples of H-atom and of alkyl radical addition to olefins to form several of the 2MH isomers. Two chemical activation systems are described here:

$$CH_3 + \text{1-hexene} \rightarrow \mathbf{1} \qquad (11)$$

$$H + \text{2-methyl-3-hexene} \rightarrow \mathbf{3} \qquad (12)$$

As mentioned earlier, **3** has only one rapid isomerization pathway, whereas **1** has three (via 5-, 6-, and 7-membered-ring transition states). The vibrational excitation energy produced by Reaction (11) is lower than that produced by Reaction (12). The simulated conditions were for 300 K, and the free radical was diluted in a great excess of argon at various pressures. To determine the sensitivity of the calculated results to the choice of energy transfer model, simulations based on Reaction (11) were carried out for the two sets of energy transfer parameters in Table VI. Both sets of parameters were determined from experiments under similar conditions on the vibrational deactivation of excited toluene by argon [18,20]. Simulations based on Reaction (12) employed only the parameters from KCSI measurements (Table VI). The duration of the simulations was chosen to be long enough so that all free-radical isomers that had not decomposed were collisionally thermalized. The calculated fractional yields of some of the products are shown as a function of collision frequency (varying argon pressure) in Figures 5, 6, and 7.

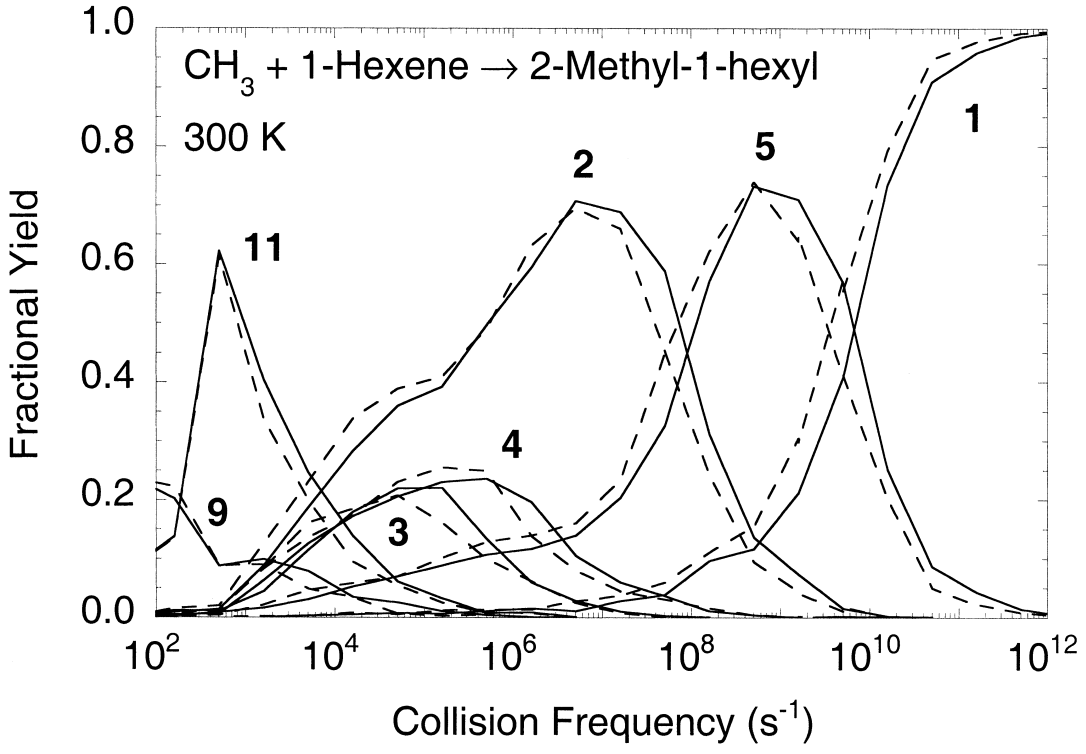

Figure 5 Yields of isomers and fragmentation products as a function of collision frequency after chemical activation of **1** via the reaction **7** → **1.** Solid lines show simulations with the generalized exponential model and KCSI parameters; broken lines show simulations with the simple exponential model and IRF parameters (see text for details).

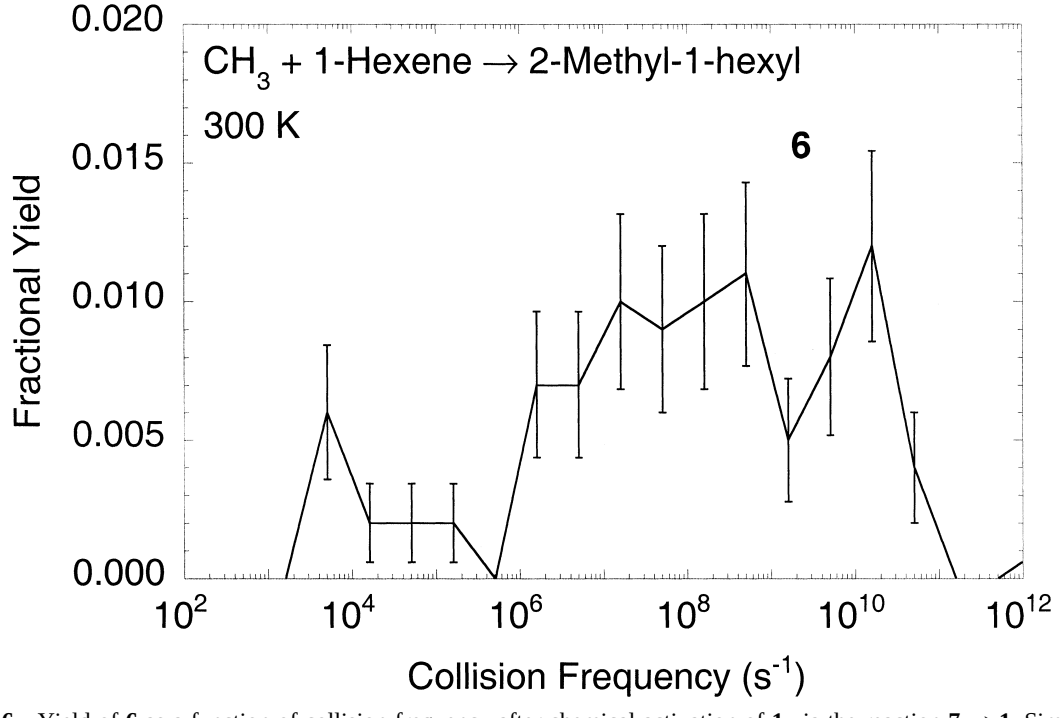

Figure 6 Yield of **6** as a function of collision frequency after chemical activation of **1** via the reaction **7** → **1.** Simulations were carried out with generalized exponential-model and KCSI parameters. Error bars show the statistical uncertainties.

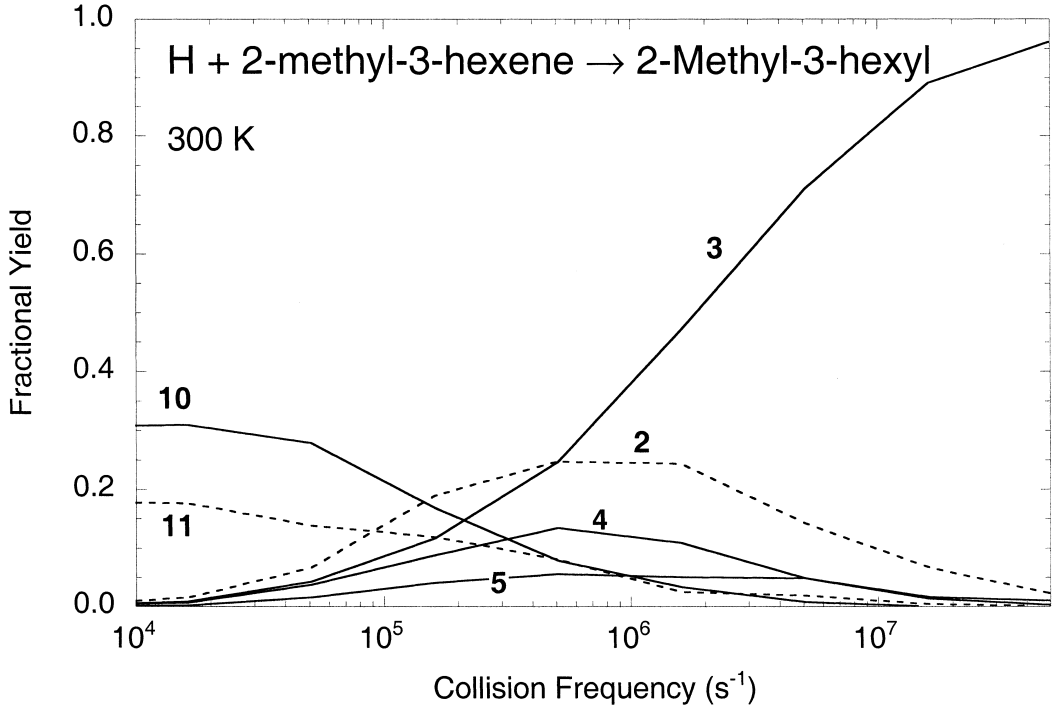

Figure 7 Yields of isomers and fragmentation products as a function of collision frequency after chemical activation of **3** via the reaction **18** → **3.** Simulations were carried out with generalized exponential-model and KCSI parameters.

The results for chemically activated **1** in Figure 5 exhibit an interesting pattern. The same qualitative behavior was calculated for formation of **1** via the more exothermic Reaction (10a), but the collision frequency corresponding to a given isomer was higher. The yields of several of the isomers can be "selected" by controlling the collision frequency (argon pressure). This behavior can be explained as follows. Isomerization of **1** to form **5** via a 6-membered-ring transition state is very rapid, because of the low energy barrier (see Figs. 2 and 3). Collisional deactivation can only compete with this isomerization at the highest collision frequencies. As the collision frequency is lowered, isomerization competes and the yield of **5** increases. The reverse isomerization is also very rapid, and therefore **1** and **5** approach equilibrium with each other. Because **5** has a lower heat of formation than **1** (see Fig. 3), the concentration of **5** is larger than **1** at equilibrium. However, as the collision frequency is lowered further, the slower **5** → **2** isomerization can take place, explaining the production of **2** (the most stable isomer) at collision frequencies around 10^7 s^{-1}. At still lower collision frequencies, the excited species have still more time for further isomerizations to compete with collisional deactivation. The reaction sequence is less clear at lower collision frequencies. Isomers **3** and **4** appear in significant yields only at relatively low collision frequencies because they are not connected by fast processes to the more abundant isomers. At very low collision frequencies, decomposition products dominate the yield spectrum. For clarity, only one set of decomposition products is shown in Figure 5, although, in fact, several sets of products are of comparable importance. Note that stabilization of excited species by spontaneous infrared emission [32,33] has been neglected in this version of MultiWell, and thus the yields estimated at low collision frequencies should be regarded as lower limits.

The choice of energy transfer parameters does not strongly affect the results shown in Figure 5. This is because the two sets of parameters give comparable values for the average energy transferred per collision at high energies and not many collisions are needed for deactivation of the isomers to energies below the reaction barriers.

The yield of **6** at high collision frequencies (Fig. 6) reflects its rapid production via the 7-membered cyclic isomerization from **1.** Because of the fast 6-membered cyclic isomerization of **6** to **2,** the magnitude of the yield of **6** is not large, however. At lower collision frequencies, **6** is still produced, but this time via the isomerization *from* **2.** Again, the yield of **6** is not large, because **2** has a lower heat of formation and because both isomers decompose to produce fragmentation products.

The second chemical activation route described here is the production of **3** via the reverse of Reaction (12). The fastest isomerization that **3** can undergo involves a 5-membered cyclic transition state, which is significantly slower than the 6-membered cyclic isomerizations of **1** and **2** described earlier. At collision frequencies low enough for the isomerization reaction to compete with collisional stabilization, the fragmentation reactions are already competitive, as shown in Figure 7. As soon as **3** isomerizes to produce **6,** the latter radical isomerizes to produce **1** and **2.** These also isomerize rapidly to produce **4** and **5.** Thus, all of the isomers appear simultaneously as **3** is lost. All of the isomers can decompose via C—C and C—H bond fission to produce fragmentation products. All of the yields are comparable at collision frequencies between 10^5 and 10^6 s^{-1} because the first isomerization reactions involving **3** are the slowest steps of the sequence.

The limited experimental data [5] on the reactions of chemically activated **3** are qualitatively consistent with model simulations. In the experiments, **3** was produced by the reverse of Reaction (17) in a bath consisting of H_2 at room temperature. The results were reported as the ratio of stabilized **3** to the yield of **10** (the S/D ratio) as a function of total pressure. We carried out simulations of this chemical activation reaction in an *argon* bath, and the results were in good agreement with the experiments. As in the experiments, the S/D ratio was found to be proportional to pressure over the range 1–64 Torr, but the simulated ratio was about a factor of 3 higher than the experiments. This agreement is surprisingly good, considering that argon collisions were simulated instead of H_2 and the reaction rate constants were predicted by theoretical calculations— not from experiments. The factor of $\times 3$ could be eliminated in the simulations by making minor changes to the energy transfer and rate constant parameters (including careful attention to the differences in rate constants for formation of *cis* and *trans* isomers of the olefins), but the additional information gained from such an exercise would be very limited.

The clear sequence of reaction yields in Figure 5 is the result of the relative rates of the reactions involved. The first reactions involving **1** are faster than the subsequent steps, which, in turn, are faster than the later steps, and so on. This relative ordering allows the system to produce the yield sequence shown. When the first reaction step has a slower rate constant than subsequent steps, then all of the reaction products appear together and no sequence is apparent. This is the case for **3.** Thus, Figures 5 and 7 illustrate two cases of relative ordering of the reaction rate constants.

Shock Wave Excitation

Prior to the arrival of a shock wave, the translational and vibrational temperatures are equal to each other. When the shock arrives, the translational temperature rises extremely rapidly due to adiabatic compression, while slow collisional energy transfer limits the rate of the vibrational energy increase. In the calculations, this situation was simulated by assuming that a reactant alkyl radical is initially described by a high translational temperature (T_{trans}) and a Boltzmann vibrational distribution at 300 K (T_{vib}). During the simulation, the vibrational energy increases due to collisional energy transfer and the alkyl radicals undergo isomerization and fragmentation reactions. Eventually, the vibrational energy distribution reaches a steady state: The rate of collisional energy transfer matches the rate of unimolecular reaction. Thus, the shock wave simulations describe the approach to steady state (including vibrational relaxation and incubation times) as well as the steady-state unimolecular reaction rate constant "fall-off" [25,26]. These simulations are very demanding because they require reaction rate constants and energy transfer data over a very wide range of vibrational energy.

Convergence Tests. Only an abbreviated series of convergence tests was carried out because it quickly became apparent that the chemical activation system provided a more stringent case. The tests confirmed that the parameters adopted for the chemical activation series are also suitable for the shock wave simulations.

Shock Wave Simulations. After passage of a shock wave, but before energy transfer takes place, the vibrational energy is the initial thermal energy characterized by T_{vib}. The vibrational energy is no longer in equilibrium with the translational temperature, and collisional activation dominates over deactivation. Low on the energy ladder, the average collisional energy transfer step size is quite small for the models in Table VI, and thus many collisions are required for collisional activation, as shown in Figure 8. In both cases, the average internal energy increases at a rate that can be characterized by a time constant. Because of the different step-size distributions, energy transfer derived from the KCSI measurements is almost four times as efficient as that derived from the IRF measurements. This behavior is closely analogous to that described by simulations [20] of the original vibrational deactivation experiments. The differences between the two energy transfer models accumulate because of the many collisions (Figure 8) required for vibrational excitation. This result demonstrates that

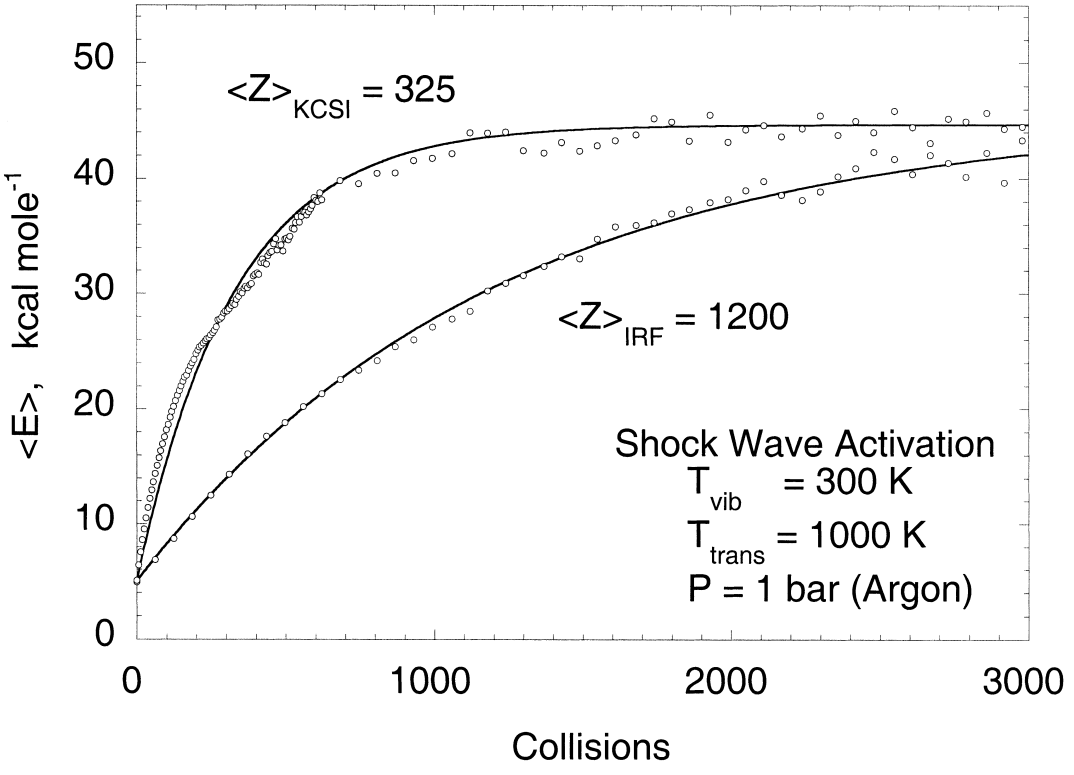

Figure 8 Average internal energy as a function of the number of collisions for two energy transfer models (see text for details). $< Z >$ denotes the average number of collisions corresponding to the vibrational relaxation time.

shock wave experiments are more demanding of high-accuracy data, but they also can provide a sensitive means for measuring energy transfer.

For both energy transfer models, the relatively slow vibrational excitation rate produces a delay (the "incubation time") in the onset of the chemical reactions, as has been seen in previous model calculations [34,25,26] and in experiments [35,36]. This delay is apparent in Figure 9, which shows the relative concentrations of various species as a function of time. In this simulation, the very low pressure (0.001 bar) emphasizes the incubation time and approach to steady state, which are much faster at higher pressures. The solid and dashed curves show the simulations based on the KCSI and IRF models, respectively. It is clear that the initial reactant (**1**) begins to isomerize and final decomposition products appear considerably earlier, according to the KCSI model.

Because of the incubation delay, the initial reaction rates are vanishingly small. As the vibrational energy approaches a steady state, the unimolecular reaction rates also increase and approach steady state. Figure 10 shows the initial increase in the instantaneous average (over energy) rate constant (see Article I) while the vibrational energy distribution is still evolving. At longer times, the average rate constants become essentially independent of time, corresponding to the usual steady-state unimolecular reaction rate constants in the fall-off regime. Note, however, that these reactions are closely coupled, and therefore the steady-state energy distributions, and hence the rate constants, are affected by *all* of the reactions.

By varying the argon pressure, the steady-state unimolecular rate constants can be determined as a function of pressure and "fall-off" curves can be constructed (Figure 11). Arrhenius plots, such as Figure 12, can be constructed for each argon pressure. In Figure 12, the curvature in the Arrhenius plots is due to the fall-off discussed above. Strong curvature is common even for single-channel reactions at high temperature and moderate pressures, where fall-off is important [8–10,35].

The usual fall-off curve for a single-channel unimolecular reaction displays three regimes. In the low-pressure regime, the rate constant is directly proportional to pressure. In the high-pressure regime, the rate constant is independent of pressure. In the fall-off regime, the rate constant makes the transition smoothly between the low-pressure and high-pressure regimes. In the coupled system, the fall-off curves are more complicated, as shown in Figure 11. Rate constant k_{51} (reaction **1** → **5**) and rate constant k_{61} (reaction **1** →

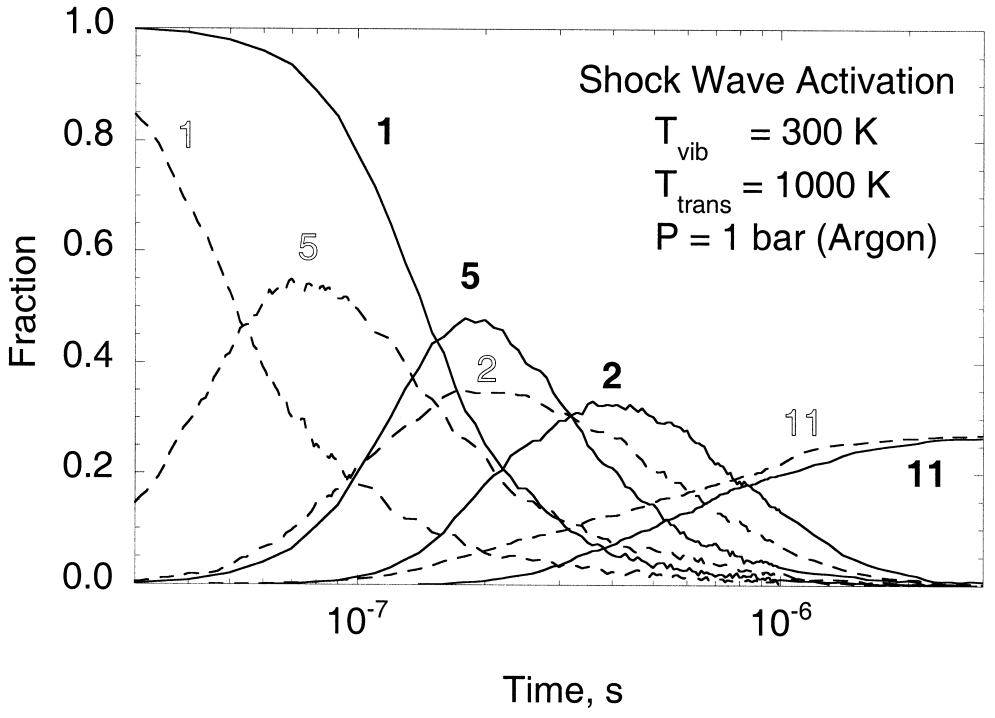

Figure 9 Fractional populations of isomers and fragmentation products as a function of time after shock excitation of **1** (see caption of Fig. 5).

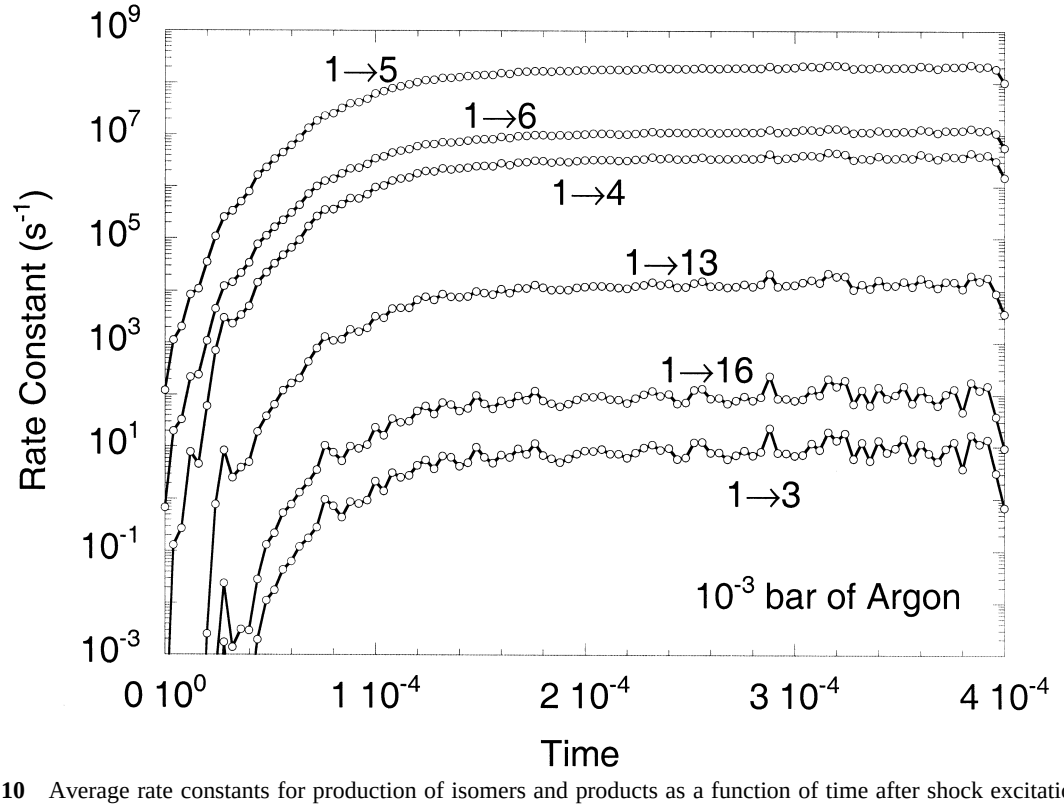

Figure 10 Average rate constants for production of isomers and products as a function of time after shock excitation of **1.** Simulations were carried out with generalized exponential-model and KCSI parameters.

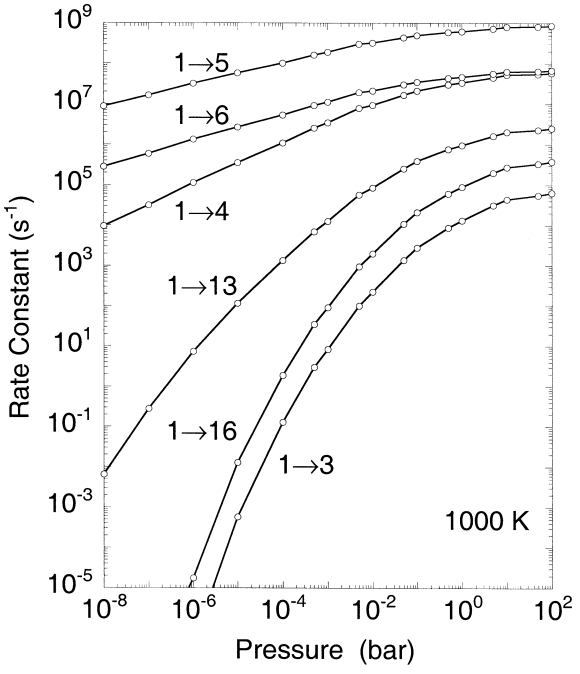

Figure 11 Fall-off curves of the steady-state rate constants for production of isomers and products from **1** at 1000 K. Simulations were carried out with generalized exponential-model and KCSI parameters.

6) both appear to follow the usual behavior described above: They show a smooth transition from first-order to zero-order. Rate constant k_{41} behaves differently: At low pressure it appears to be nearly second-order, and it then makes a smooth transition to zero-order. Each successively slower rate constant appears to be of higher order at low pressure, and each smoothly makes a transition to zero-order at high pressure.

This unusual fall-off behavior is due to the depletion of population at higher energies by the (fast) reactions that have lower energy thresholds. It is a direct consequence of the coupling among the multiple reaction channels. In the high-pressure limit, energy transfer can maintain the thermal distribution function and there is no population depletion at high energy. Under these conditions, all reactions are in the high-pressure limit. At somewhat lower pressures, the reactions with low energy thresholds deplete the high-energy population distributions, and hence the reactions with high-energy thresholds are greatly slowed. This effect can be illustrated qualitatively with a Lindemann-type mechanism that describes the unimolecular decomposition of reactant A via two reaction channels:

$$\mathrm{A} + \mathrm{M} \leftrightarrow \mathrm{A}^* + \mathrm{M} \qquad \text{(a,-a)}$$

$$\mathrm{A}^* + \mathrm{M} \leftrightarrow \mathrm{A}^{**} + \mathrm{M} \qquad \text{(b,-b)}$$

$$\mathrm{A}^* \rightarrow \mathrm{P_c} \qquad \text{(c)}$$

$$\mathrm{A}^{**} \rightarrow \mathrm{P_c} \qquad \text{(d)}$$

$$\mathrm{A}^{**} \rightarrow \mathrm{P_e} \qquad \text{(e)}$$

where M is a collider gas, successive vibrational excitation is denoted by successive asterisks, and P_c and P_e are products. The rates of production of P_c and P_e can be obtained by using a pseudo-steady-state analysis for [A*] and [A**]. The results can be expressed as the rate of production of product P_c and the ratio of the production rates:

$$\frac{d[\mathrm{P_c}]}{dt} = \left\{ k_c + \frac{k_b k_e [\mathrm{M}]}{k_{-b}[\mathrm{M}] + k_d + k_e} \right\} \left\{ \frac{k_a[\mathrm{M}]}{(k_{-a} + k_b)[\mathrm{M}] + k_c - \dfrac{k_b k_{-b}[\mathrm{M}]^2}{k_{-b}[\mathrm{M}] + k_d + k_e}} \right\} \qquad (13)$$

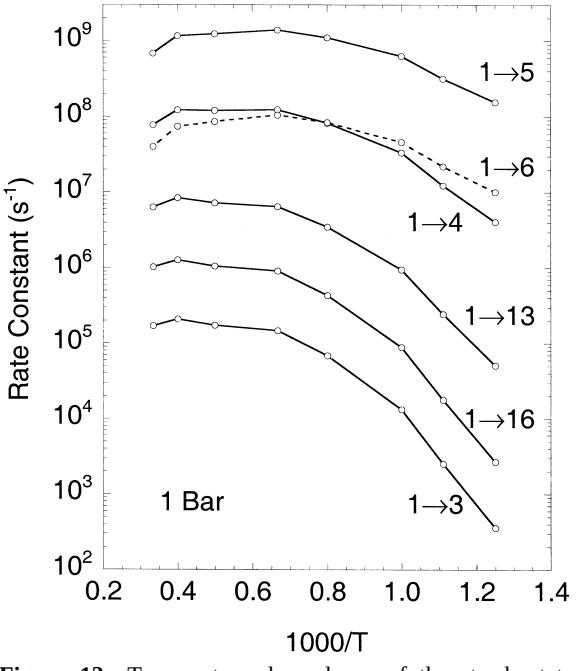

Figure 12 Temperature dependence of the steady-state rate constants for production of isomers and products from **1** at the pressure of 1 bar (argon). Simulations were carried out with generalized exponential-model and KCSI parameters.

$$\frac{d[P_e]/dt}{d[P_c]/dt} = \frac{k_b k_e[M]}{k_c(k_{-b}[M] + k_d + k_e) + k_b k_d[M]} \quad (14)$$

where [M] is the concentration of M. The ratio of the production rates is pressure-dependent, showing that the fall-off curves are different for the two products. In the low-pressure limit, the rate of production of product P_c is directly proportional to [M], whereas that for product P_e depends on $[M]^2$.

This simple mechanism illustrates qualitatively the effects seen in Figure 11 for the far more complex 2MH system. The higher-order dependence on [M] exhibited by many of the reactions in Figure 11 is expected to be present to a greater or lesser degree in all unimolecular systems with multiple reaction channels. In the 2MH simulations, many weak collisions are needed for thermal activation of the alkyl radicals to the lowest reaction threshold, and many more collisions are needed for activation to the next threshold, etc. Furthermore, multiple isomerization reactions take place concurrently with the fragmentation reactions. Because of these complexities, the pressure dependence of the 2MH reactions in the low-pressure limit is more complex than the simple first- and second-order dependence on [M] predicted by Eqs. (13) and (14). In order for the effect to be apparent, the reaction thresholds must be widely separated, but this produces rate constants that differ very widely in magnitude (see Fig. 11), which are not amenable to experimental study. In systems that have nearly identical reaction thresholds, the rate constants are of similar magnitude, but the higher-order pressure dependence has not been observed experimentally [37–39].

CONCLUSIONS

The master equation simulations presented here are model calculations based on *ab initio* and density functional electronic structure calculations from the literature. Furthermore, energy transfer data are not available and arbitrary assumptions were needed in order to carry out the master equation calculations. Nevertheless, the qualitative results are in good agreement with experiments that were carried out on analogous alkyl radical systems and on chemically activated reactions of **3** [5]. The results reveal several interesting properties of coupled reactions.

The yields in a given chemical activation system correspond closely to the sequence of the appearance of intermediate products in the same system activated by shock waves. Both types of activation produce a very regular appearance of isomers when the first isomerization steps are faster than subsequent steps. The fortuitous ordering of the isomerization rates of **1** produces exceptionally regular behavior in both the chemical activation and the shock wave activation systems. In contrast, the first isomerization steps involving **3** are slower than the subsequent steps and all of the product isomers appear simultaneously. In all cases, the results are qualitatively in agreement with those of earlier workers, who described the rapid "identity scrambling" of chemically activated alkyl radicals [30].

The unimolecular rate-constant fall-off curves showed the effects of the coupled multiple reaction channels. In particular, the isomerization reaction rate constants are not second-order at low pressure, in contrast to the pressure dependence expected for single-channel reactions. In the coupled system, the reactions with higher threshold energies react more slowly than in the uncoupled system at the same pressure, because the reactions with lower threshold energies deplete the higher-energy population distributions. The coupling produces fall-off curves that have a higher-order [M] dependence in the low-pressure limit. This effect can only be simulated by including the coupled pathways. It will be present in all multiple-channel unimolecular reaction-channel systems and may have important effects on the rate constants in those systems.

We are grateful to George Lendvay for communicating the vibrational frequencies for the structures reported in [3]. Acknowledgment is made to the donors of The Petroleum Research Fund, administered by the ACS, for partial support of this research. N.F.O. is grateful for funding from the General Electric Undergraduate Research Program at the University of Michigan. Thanks also go to Laurie M. Yoder and Keith D. King for carefully reading the manuscript and making helpful suggestions. J.R.B. thanks William L. Hase and the Chemistry Department at Wayne State University for their hospitality during a sabbatical visit.

BIBLIOGRAPHY

1. Barker, J. R. Int J Chem Kinet 2001, 33, 232.
2. Barker, J. R. MultiWell; 1.01 ed.; http://aoss.engin.umich.edu/multiwell/: Ann Arbor, MI, 1999.
3. Viskolcz, B.; Lendvay, G.; Seres, L. J Phys Chem A 1997, 101, 7119.
4. Yamauchi, N.; Miyoshi, A.; Kosaka, K. J Phys Chem A 1999, 103, 2723.
5. Larson, C. W.; Rabinovitch, B. S.; Tardy, D. C. J Chem Phys 1967, 47, 4570.
6. Lendvay, G. Vibrational Frequencies for the 2-Methylhexyl Free Radical Isomers and Isomerization Transition States.

7. Pople, J. A.; Scott, A. P.; Wong, M. W.; Radom, L. Isr J Chem 1993, 33, 345.
8. Robinson, P. J.; Holbrook, K. A. Unimolecular Reactions; Wiley-Interscience: New York, 1972.
9. Forst, W. Theory of Unimolecular Reactions; Academic Press: New York, 1973.
10. Gilbert, R. G.; Smith, S. C. Theory of Unimolecular and Recombination Reactions; Blackwell Scientific: Oxford, 1990.
11. Baer, T.; Hase, W. L. Unimolecular Reaction Dynamics. Theory and Experiments; Oxford University Press: New York, 1996.
12. Benson, S. W. Thermochemical Kinetics, 2nd ed.; Wiley: New York, 1976.
13. Forst, W. J. J Phys Chem 1983, 83, 100.
14. Troe, J. J. J Chem Phys 1977, 66, 4758.
15. Perry's Chemical Engineer's Handbook, 6th ed.; Green, D. W.; Maloney, J. O., Eds.; McGraw-Hill, Inc.: New York, 1984.
16. Barker, J. R.; Yoder, L. M.; King, K. D. J Phys Chem A 2000, in press.
17. Toselli, B. M.; Brenner, J. D.; Yerram, M. L.; Chin, W. E.; King, K. D.; Barker, J. R. J Chem Phys 1991, 95, 176.
18. Barker, J. R.; Toselli, B. M. Int Rev Phys Chem 1993, 12, 305.
19. Linhananta, A.; Lim, K. F. J Phys Chem Chem Phys 1999, 1, 3467.
20. Lenzer, T.; Luther, K.; Reihs, K.; Symonds, A. C. J Chem Phys 2000, 112, 4090.
21. Hold, U.; Lenzer, T.; Luther, K.; Reihs, K.; Symonds, A. C. J Chem Phys 2000, 112, 4076.
22. Barker, J. R. J Chem Phys 1983, 77, 301.
23. Barker, J. R. J Phys Chem 1984, 88, 11.
24. Shi, J.; Barker, J. R. J Chem Phys 1988, 88, 6219.
25. Shi, J.; Barker, J. R. Int J Chem Kinet 1990, 22, 187.
26. Barker, J. R.; King, K. D. J Chem Phys 1995, 103, 4953.
27. Gillespie, D. T. J Comp Phys 1976, 22, 403.
28. Gillespie, D. T. J Phys Chem 1977, 81, 2340.
29. Gillespie, D. T. J Comp Phys 1978, 28, 395.
30. Larson, C. W.; Chua, P. T.; Rabinovitch, B. S. J Phys Chem 1972, 76, 2507.
31. Tardy, D. C.; Rabinovitch, B. S. Chem Rev 1977, 77, 369.
32. Durana, J. F.; McDonald, J. D. J Chem Phys 1977, 64, 2518.
33. Barker, J. R. J Phys Chem 1992, 96, 7361.
34. Dove, J. E.; Troe, J. J Chem Phys 1978, 35, 1.
35. Kiefer, J. H.; Kumaran, S. S.; Sundaram, S. J Chem Phys 1993, 99, 3531.
36. Fulle, D.; Dib, A.; Kiefer, J. H. J Phys Chem A 1998, 102, 7480.
37. Gaynor, B. J.; Gilbert, R. G.; King, K. D. Chem Phys Lett 1978, 58, 591.
38. King, K. D.; Gaynor, B. J.; Gilbert, G. G. Int J Chem Kinet 1979, 11, 11.
39. King, K. D. Studies of Collisional Energy Transfer Using Pressure-Dependent Very Low-Pressure Pyrolysis (VLPP); In Advances in Chemical Kinetics and Dynamics. Vol. 2A. Vibrational Energy Transfer Involving Large and Small Molecules; Barker, J. R., Ed.; JAI Press: Greenwich, 1995; Vol. 2A; pp 171–208.